Classification of ablation mode during impact of hot liquid jet on a solid

A. Lecoanet, F. Payot, C. Journeau, N. Rimbert, Michel Gradeck

Version of Record: https://www.sciencedirect.com/science/article/pii/S0017931021009881
Manuscript_2e1cf489fc01323d838925c9a2832f6c

Classification of ablation mode during impact of hot liquid jet on a solid

A. Lecoanet[a,b], F. Payot[c], C. Journeau[a], N. Rimbert[b], M. Gradeck[b,*]

[a] *CEA, DES, IRESNE, DTN, SMTA, Severe Accident Experimental Laboratory, Cadarache F-13108 Saint-Paul-Lez-Durance, France*
[b] *Université de Lorraine, CNRS, LEMTA, F-54000, Nancy, France*
[c] *CEA, DES, IRESNE, DER, Cadarache F-13108 Saint-Paul-Lez-Durance, France*

Abstract

The ablation consecutive to hot jet impingement is a safety issue for future Sodium Fast Reactors (SFR) core-catcher that can occur during relocation of molten fuel (corium) under severe nuclear accident situation. Much is still unknown on the ablation phenomenon especially explanations on cavity shape are lacking. However, these data are required to specify the core-catchers which will be used in future nuclear reactors' vessel to prevent the corium from drilling through the confinement vessel during severe accident. To tackle this subject, data from experiments are obtained and analyzed to identify first order physical mechanisms at stake, and their links to geometry of the cavity. Two ablation mechanisms are noticed, the film ablation regime, for which liquid exits the cavity as a liquid film followed by the pool effect for which the cavity is filled with liquid. The analysis of results shows that the cavity shape is fixed during the film ablation regime and translates as ablation proceeds. Modes of liquid exit from the cavity are analyzed as well as the shapes the cavity assumes. Liquid/air interface temperature is also determined, in the film ablation regime. An explanation of cavity shape is presented. Conditions based on dimensionless numbers are put forward to differentiate between different cavity shapes and liquid exit modes. A first model for transition between film and pool effect ab-

*Corresponding author
Email address: michel.gradeck@univ-lorraine.fr (M. Gradeck)

lation regimes is presented. It is the first time to the best of our knowledge that such analyses are undertaken. These give new tools for ablation risk assessment.

Keywords: Ablation, Cavity shape, Liquid jet, fluid-structure interaction, nuclear safety

---

1. Nomenclature

Latin letters

B	Melting number	$\frac{C_{p,j}(T_j - T_{f,s})}{L + C_{p,s}(T_{f,s} - T_{0,s})}$	-
C_p	Specific heat	-	$J.kg^{-1}.K^{-1}$
D_j	Jet diameter	-	m
Fr	Froude number	$\frac{V_j}{\sqrt{gD_j}}$	-
g	Gravity acceleration	9.81	$m.s^{-2}$
h	Convective heat transfer coefficient	-	$W.m^{-2}.K^{-1}$
h_f	h with melting	-	$W.m^{-2}.K^{-1}$
k_j	Thermal conductivity of the jet	-	$W.m^{-1}.K^{-1}$
l	Liquid layer thickness	-	m
L	Latent heat of fusion	333 700 (ice [1])	$J.kg^{-1}$
Nu	Nusselt number	$\frac{hD_j}{k_j}$	-
Oh	Ohnesorge number	$\frac{\mu_j}{\sqrt{\rho_j \sigma_j D_j}} = \frac{\sqrt{We}}{Re}$	-
Pr	Prandtl number	$\frac{\mu_j C_{p,j}}{k_j}$	-
Re	Reynolds number	$\frac{\rho_j V_j D_j}{\mu_j}$	-
r	Radial distance from jet axis	-	m
r^*	Dimensionless radial distance	$\frac{r}{D_j}$	-
St	Stanton number	$\frac{h_f}{V_j \rho_j C_{p,j}} = \frac{Nu}{RePr}$	-
t	Time	-	s
t^*	Dimensionless time	$\frac{t}{t_{PE}}$	-
T	Temperature	-	K
V	Velocity	-	$m.s^{-1}$
V_j	Jet velocity at impact	-	$m.s^{-1}$

V_f	Ablation velocity	-	$m.s^{-1}$
We	Weber number	$\frac{\rho_j V_j^2 D_j}{\sigma_j}$	-
Z	Cavity depth	-	m
Z^*	Relative depth at pool effect appearance	$\frac{Z_{PE}}{D_j}$	-
Greek letters			
α	Side angle of the truncated cone shape	-	^{o}
Δ	Absolute uncertainty	-	-
μ	Dynamic viscosity	-	$Pa.s$
ν	Cinematic viscosity	$\frac{\mu}{\rho}$	$m^2.s^{-1}$
ρ	Density	-	$kg.m^{-3}$
σ	Surface tension	-	$N.m^{-1}$
Indices			
0	Initial		
e	Entrance		
exp	Experimental		
f	Fusion		
j	Jet		
max	Maximum value		
PE	Pool effect		
s	Solid		
$stag$	Stagnation zone		
sys	Related to experimental setup limitations		

2. Glossary

$ESFR-SMART$	European Sodium Fast Reactor - Safety Measures Assessment and Research Tools
Exp. ref.	Experiment reference as given in table 3
$HAnSoLO$	Hot AblatioN of a SOlid by a Liquid – Observations

IR	InfraRed
$LEMTA$	*Laboratoire Énergies & Mécanique Théorique et Appliquée*
SFR	Sodium Fast Reactor

3. Introduction

. The ablation process (*i.e.* drilling by phase change) can be encountered in nuclear safety study. Indeed, during a postulated severe accident with core melting in a nuclear reactor, a corium[1], could form and flow downward driven by gravity. Consequently a jet of corium can impact a metallic structure, such as the core-catcher which is located under the reactor core. The core-catcher, which is designed to collect, maintain and cool the molten fuel, could be ablated by the aforementioned corium jet [2]. This possibility is taken into account in the early design stages of most of the new nuclear reactors [3, 4]. This issue had been studied for the jet ablation of concrete in the 3$^{\text{rd}}$ generation (*i.e.* EPR) [5] and is now considered for core-catchers of the 4$^{\text{th}}$ generation of nuclear reactors which must represent a scale up on safety [6].

Ablation can also occur in nature, during for instance the fall of an ice body through the atmosphere [7]. Ablation of solid structures by hot free liquid jets is also encountered in human operations, like cutting of ice, or permafrost by water jet [8, 9, 10]. These operations are conducted to access subglacial environments in arctic for research purpose, to free the way of ships or dig the ground.

. Roberts [7] is the first author who studied the ablation of a solid structure by the flow of a hot fluid around a stagnation point, as can be encountered close to the impact point of a jet. His study was theoretical and he considered the fluid to be gaseous (*i.e.* air). Gilpin and Lipsett [11, 12, 13] studied the ablation of a structure by a hot liquid jet. They have shown the existence of a flat stagnation zone followed by an inflection of the cavity. The transposition of Robert's work

[1] The corium is a magma composed of molten fuel and liquid steel.

to the case of a liquid jet impacting a structure was achieved by Swedish *et al.* [14].

. Lipsett, Gilpin and Swedish *et al.* [11, 12, 13, 14] performed some experimental work. However, these results were obtained with upward flowing jet. The jets they used were laminar. Also, concerning cavity shape analysis, the ones performed by Lipsett and Gilpin [11, 12] were based on post-trial cross-sections, and Swedish *et al.* [14] study was focused on the stagnation zone. In the scope of nuclear safety studies, these data were complemented by Furutani *et al.* [15], Saito *et al.* [16] and Sato *et al.* [17]. Their focus was on the maximum penetration velocity. They did not analyze the cavity shape but gave post-trial cross-sections results. However, Saito *et al.* [16] identified a succession of two ablation regimes: the film regime which is followed by the pool effect. These two regimes are represented schematically in Fig. 1 along with the relevant variables for the present study. The liquid flows over the solid within the cavity as a liquid film in the film regime. The pool effect occurs when the film of liquid flowing out of the cavity during the film regime collapses down in the cavity. The liquid jet then impacts a pool of liquid.

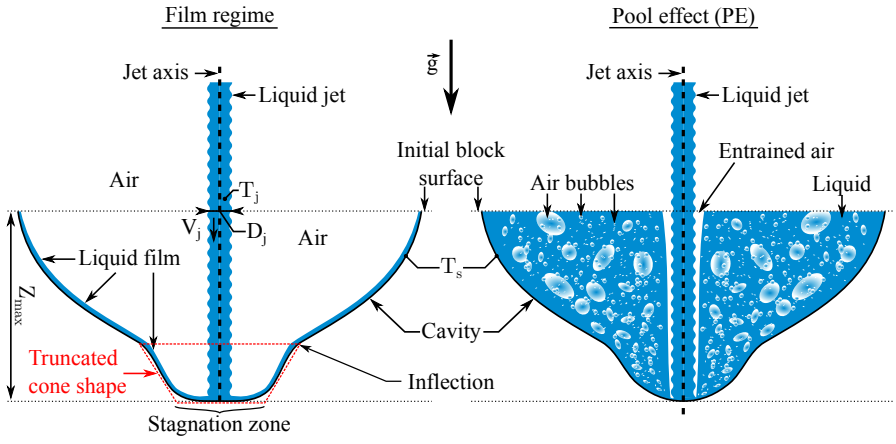

Figure 1: Schematic depiction of the cavity produced by ablation during both film and pool effect regimes, with the relevant variables, and cavity zones, highlighted.

. In order to link the ablation velocity to the heat transfer at impact, numerous authors [7, 11, 14, 16, 17, 15, 18] made use of a jump condition on enthalpy, assuming constant ablation velocity and Newton's law for heat transfer on liquid side. These assumptions lead to equation (1) in which, h_f is the convective heat transfer coefficient during ablation in jet stagnation zone, V_f is the ablation velocity, ρ_s is the density of the solid, L is the latent heat of fusion, $C_{p,s}$ is the heat capacity of the solid. Likewise, T_j is the temperature of the jet, $T_{0,s}$ is the initial temperature of the solid and $T_{f,s}$ is the melting temperature of the solid.

$$h_f \left(T_j - T_{f,s}\right) = V_f \rho_s \left[L + C_{p,s} \left(T_{f,s} - T_{0,s}\right)\right] \tag{1}$$

The latter equation (1) can be scaled by $\rho_j V_j$. Doing so leads to equation (2), in which $St = \frac{h_f}{\rho_j V_j C_{p,j}}$ is the Stanton number and $B = \frac{C_{p,j}(T_j - T_{f,s})}{L + C_{p,s}(T_{f,s} - T_{0,s})}$ is the melting number. The latter number (B) is encountered when the heat transfer is studied when melting occurs [19]. It was used by Griffin [19] to study melting of glacial ice, and by Epstein [20] to link Nusselt numbers obtained at the impact of a jet onto a solid when melting occurs to the one obtained when the solid does not melt. Eq. (2) demonstrates that the mass flow of solid material ablated is proportional to the mass flow of the jet material, to the Stanton number which compares the heat transfer at the interface with the specific heat brought by the jet, and to the melting number which compares the heat brought by the jet to the heat required to melt the solid.

$$\frac{\rho_s V_f}{\rho_j V_j} = StB \tag{2}$$

. Eq. (1) can be used to compute a Nusselt number $\left(Nu = \frac{hD_j}{k_j}\right)$ from ablation velocity V_f. A significant part of the studies conducted on ablation of a solid by a liquid jet focused on determining a Nusselt number at the jet impact for design purpose [21, 11, 16, 17, 18]. As stated before, Epstein [20] proposed that Nusselt number, determined when no melting occurs, could be converted to its corresponding value when melting occurs, by means of a correction. The conversion is given by Eq. (3), where Nu is the Nusselt number without melting

and Nu_f is the one with melting. Tien *et al.* [22] demonstrated this equation theoretically for solids at their melting temperature. It was later confirmed experimentally by Swedish *et al.* [14] and more recently by ourselves [18]. Once again, the melting number is encountered, as it is a measure of the effect of melting on heat transfers.

$$Nu = \frac{B}{ln\,(1+B)} Nu_f \qquad with \qquad Nu = \frac{hD_j}{k_j}, \qquad Nu_f = \frac{h_f D_j}{k_j} \tag{3}$$

. Recently, new studies were conducted on the topic. However, these studies focus mostly on simulations [23, 24], on the ablation of a solid by a liquid jet of a different nature (*e.g.* steel impinging on concrete) [25, 24], or on fuel-coolant interaction [26]. Also, the pool effect is completely disregarded. New ways for examining the heat transfer during ablation and the progression of the ablation front were explored in recent literature. An example is the effective conductivity method [27]. In this method, the effect of melting on heat transfer inside the impinged solid is enclosed in an effective conductivity. This effective conductivity depends on the Nusselt number at impact. This method was applied to reproduce experimental results obtained using Wood's metal for both the jet and the solid. It requires data fitting to match the experimental results. It shows that it is difficult to gather precise physical knowledge on metal / metal experiments. An *et al.* [25] modeled the progression of the ablation front making the hypothesis that transfers between the jet and the solid were driven by radiation. They concluded that the approach assuming forced convection dominated heat transfer is closer to their experimental results. Concerning numerical simulation work, Li *et al.*[23, 24] conducted simulations using a combination of Moving Particle Semi-Implicit and Large Eddy Simulation methods. They were able [23] to reproduce the results of Sato *et al.* [17]. However, they did not report any pool effect and the shapes of cavities they obtained do not match our results [18]. This may be due to the different jet / solid systems used (Steel / Steel or Steel / Oxide for Li *et al.* [23, 24] and Water / Ice for our work.) In order to improve our knowledge of the physical phenomena at stake during

ablation of a solid structure by a liquid jet, it is chosen in the present work to conduct our experiments on a system allowing for fine scrutiny of the cavity shape as well as heat transfers.

. Therefore, to study the ablation of a solid by a liquid jet, a dedicated experimental setup was built in LEMTA. In this setup, named "HAnSoLO" for "Hot AblatioN of a SOlid by a Liquid – Observations," transparent ice and water serve as impacted solid and liquid jet materials. A detailed description of the experimental setup is provided in [18, 28]. This choice gives access to the evolution of the cavity shape throughout the ablation process. Moreover, HAnSoLO setup allows for real-time recording of the cavity produced by ablation, by means of a high-speed camera and backlighting of the ice block subjected to ablation. The ice blocks used are 50 cm in length along the optical axis of the high-speed camera and 25 cm in width and height. Jet velocity may be tuned between 1 $m.s^{-1}$ and 10 $m.s^{-1}$, its temperature may be tuned between 20 ^oC and 80 ^oC. Nozzle diameters ranging from 3 mm to 10 mm may be used. It can be translated in terms of dimensionless numbers: $Re \in [4\,000 - 270\,000]$, $Pr \in [2.5 - 7.0]$ and $B \in [0.25 - 1.0]$. To complement the data acquired with the high-speed camera, surface temperature of liquid flowing over the solid is available through IR camera recording. Finally, a standard camera is used to record the ablation process from above. It allows for precise identification of ablation regime and transition determination. To the best of our knowledge, this is the first time these measurement are obtained.

Some first results were achieved with HAnSoLO setup [29, 18]. They were obtained with a nozzle diameter of 6 mm. The succession of the film ablation regime and the pool effect was witnessed for a jet temperature of 50 ^oC and a jet velocity ranging from 1.2 $m.s^{-1}$ to 10.0 $m.s^{-1}$ [29]. It was later confirmed by experiments performed with jet temperatures of 30 ^oC and 70 ^oC [18]. These studies also confirmed that ablation rate was constant throughout the film ablation regime but varies with time during pool effect. A potential increase in ablation velocity at transition to pool effect was also reported. This

increase was transient, and was followed by a decrease in ablation velocity. First analysis of the cavity shape [18] – *cf.* Fig. 1 – showed that the cavity appears flat around the impact point. The radial extent of this flat part corresponds to the stagnation zone which develops at the impact of a free axisymmetric jet on solid [30]. Away from the impact point, the cavity widens and forms a truncated cone shape – *cf.* Fig. 1. Then an inflection occurs, which can be followed by a plateau. Finally, the cavity widens again before joining the solid surface. The height of the truncated cone shape decreases as jet velocity increases [18]. These observed behaviors agree with the diagrams reported by Gilpin [11]. The plateau may come close enough to the flat part of the cavity, the one surrounding the impact point, to hide the truncated cone shape. We have concluded [18, 28] that the plateau is actually due to a local increase of the cavity depth which is hidden by the backlighting observation, as this only gives a projection of the actual cavity shape. Analysis of the ablation velocity along the jet axis revealed to us that, even if the jet is turbulent, the stagnation zone is laminar up to jet Reynolds number of at least 112 000. This is coherent with the work of Tong [31], who have reported a laminarization of the flow at the impact due to stagnation zone pressure gradient.

. In these previous studies, a dimensionless time, which used the time needed to reach the pool effect as a characteristic time scale, was used – Eq. (4). In the present study, this dimensionless expression was preferred to a more physically meaningful one, as for instance $\frac{tD_j}{V_j}$ because, we have noted that heat and mass transfers are time independent during the film regime[2]. Thus, to study ablation modes, the most significant phenomenon is the transition toward pool effect and not the shear stress at impact.

$$t^* = \frac{t}{t_{PE}} \tag{4}$$

[2]This was speculated before [18] and is shown further in the present article.

. The goals of the present piece of work are to further analyze the important features influencing the cavity shape and ablation modes that can be encountered during the ablation of a solid structure following the impact of a hot turbulent free liquid jet, by listing and quantifying them. More precisely, the focus is on distinguishing relevant dimensionless numbers and consecutively putting forward physical mechanisms explaining different cavity shapes and different ablation modes. The focus is here set on the film ablation regime and the transition to the pool effect. Therefore, the pool effect is not directly studied here. This knowledge was lacking and is important to correctly assess the shape of the cavity produced by ablation. In the field of nuclear safety, it will help with the sizing of core-catchers and, in ice drilling context, it may help with drilling site management.

. To meet these requirements, previous data gathered by the authors on HAnSoLO facility [18, 29] are presented and analyzed in this paper. Ten additional experiments were conducted to investigate the influence of the diameter on the ablation modes. Detailed summary of the experiments used for the present analyses are reported in table 3. Related uncertainties on the input parameters are reported in table 4. Across the present piece of work, nomenclature is used to name the different experiments. It consists in the concatenation of the nozzle diameter used, jet prescribed temperature and velocity. Therefore, experiment D6T50V5 was performed with a nozzle diameter of 6 mm, a jet prescribed temperature of 50 ^oC, and a jet prescribed velocity[3] of 5 $m.s^{-1}$. Likewise, position of the experiments conducted in the Reynolds number (Re) / melting number (B) domain is on display in Fig. 2. This figure shows that experimental runs are spread evenly between $B = 0.37$ and $B = 0.89$, as well as between $Re = 11\ 000$ and $Re = 147\ 000$. This choice of domain has been driven by the fact that B represents melting effect on heat transfer and Re is important for hydrodynamic characterizations. Melting numbers were kept below 1. In this case melting ef-

[3]For clarity's sake decimals were omitted.

fect is moderate and different modeling approaches give similar results in terms of the effect of melting on heat transfer - see [22].

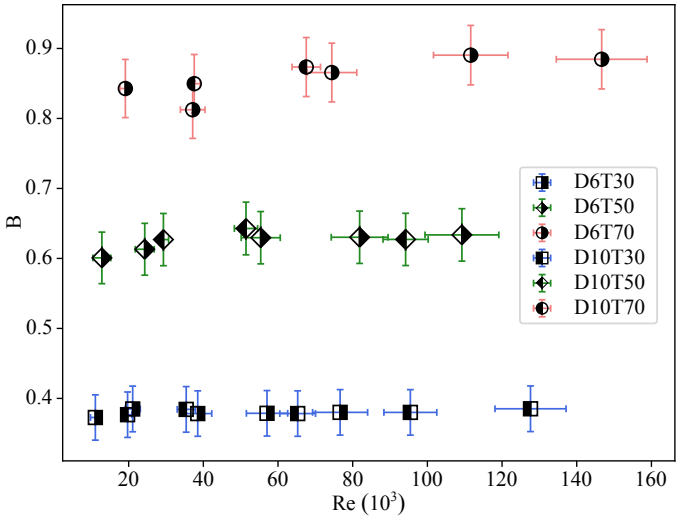

Figure 2: Location of the experiments in the Reynolds number (Re) / melting number (B) domain. Uncertainty intervals are pictured as error bars. Further information is available in table 3. Uncertainties are available in table 4.

. Firstly, we present an in-depth investigation of the evolution of the cavity shape with time throughout the film regime. The following part is devoted to an analysis of the evolution of the cavity shape with Reynolds number. Afterward, the exit state of the liquid is investigated. Criteria to predicts both the cavity shape and the exit state of the liquid are obtained. An analysis of surface temperature profiles comes after. These sections lead to an explanation of the cavity shape by means of physical mechanisms understanding. Finally, transition toward the pool effect is analyzed and a first model is put forward, which highlights the importance of $Fr = \frac{V_j}{\sqrt{gD_j}}$ for the determination of $Z^* = \frac{Z_{max,cavity}}{D_j} = \frac{Z_{PE}}{D_j}$ at the transition toward the pool effect.

To carry out this study, Python 3 was used for both the computations and graphs. We mainly used Numpy, Matplotlib and Scikit-Image [32] packages.

. The present study was achieved within the scope of ESFR-SMART European project [2, 33]. This project focuses on safety of future sodium cooled fast reactors (SFR). Such reactors must be designed to resist severe nuclear accidents with core meltdown [6], thus short- and long-term corium mitigation strategies were defined [2]. The possibility of ablation consecutive to impingement of a jet of corium onto the core-catcher or structural elements are considered and reinforcement of strategic points, those which can be directly impacted by a jet of corium, is foreseen.

4. Time evolution of cavity shape

. For each experiment, time of jet impact and pool effect transition are determined using both images from the high-speed camera and from the standard camera.

. In order to conduct a robust analysis of the cavity shape evolution during the film regime, an image processing algorithm was developed which is described in the appendix 13. It was programmed using Python 3 and Scikit-Image [32]. In the analysis, spatial extents of cavity contours obtained are dimensionless. For the radial direction, the origin is placed at jet axis and values are divided by the jet diameter at impact. For the vertical direction, the origin is placed at cavity deepest point, and values are scaled by jet diameter.

. Examples of representative contours obtained in film ablation regime are gathered in Fig. 3. For each experiment, contours for $t^* = 0.50$; 0.60; 0.70; 0.80; 0.90 are given. The first interesting result is that contours for each experiment overlap. Cavity seems to move deeper into the solid but keeps its shape. This is a confirmation of what we inferred in an earlier study [18]. It clearly shows that transfers occur at quasi-steady state. The inflection point described before, in introduction of this article and further in detail in [18], appears at a fixed distance from the impact point.

Furthermore, one can notice that for a given jet diameter the inflection point and plateau occur closer to the impact point as jet Reynolds number increases. It is consistent with Gilpin's results [11][4]. In his study he noted that cavities issued from ablation are divided in two parts: a smooth part which begin at jet impact to which succeeds, as we look further from the impact point, a rough part. Gilpin [11] gave diagrams[5], which showed that the height of the smooth part decreases as jet Reynolds number increases. He explained the transition between these two parts by way of onset of a hydraulic jump onset. We challenge this affirmation as no hydraulic jump was witnessed on visualization of the block surface by both the camera filming the block surface or the experimenters during experiments. Our explanation is provided further in the article – *cf.* section 8.

Additionally, the end of the plateau occurs at $r^* \approx 4.5$. According to Lienhard [34], this corresponds to the distance at which droplets depart from the flowing liquid films produced by the impact of a turbulent liquid jet onto a solid plate.

. Two experiments do not comply with the above description. Corresponding contours are available in Fig. 4. Contours overlap only up to the infection point. However, this does not challenge our conclusions as, when these deviations are witnessed, the liquid exits the cavity as a coherent liquid sheet. Instead, it shows the effect of liquid exit state on cavity shape. It is discussed in section 6. We have noticed visually that coherent liquid sheets tend to detach from the solid at the inflection point. This is precisely, where cavity depth locally increases as described in [18]. When a sheet appears, liquid is not in contact with the solid after this point, solid melting stops and cavity shape changes.

[4]Gilpin [11] performed experimental work on ablation of an ice block by a liquid jet. In his experimental setup, the bloc was impacted from below.

[5]Unlike experiments performed here, contours obtained by Gilpin [11] were provided by post-mortem examinations.

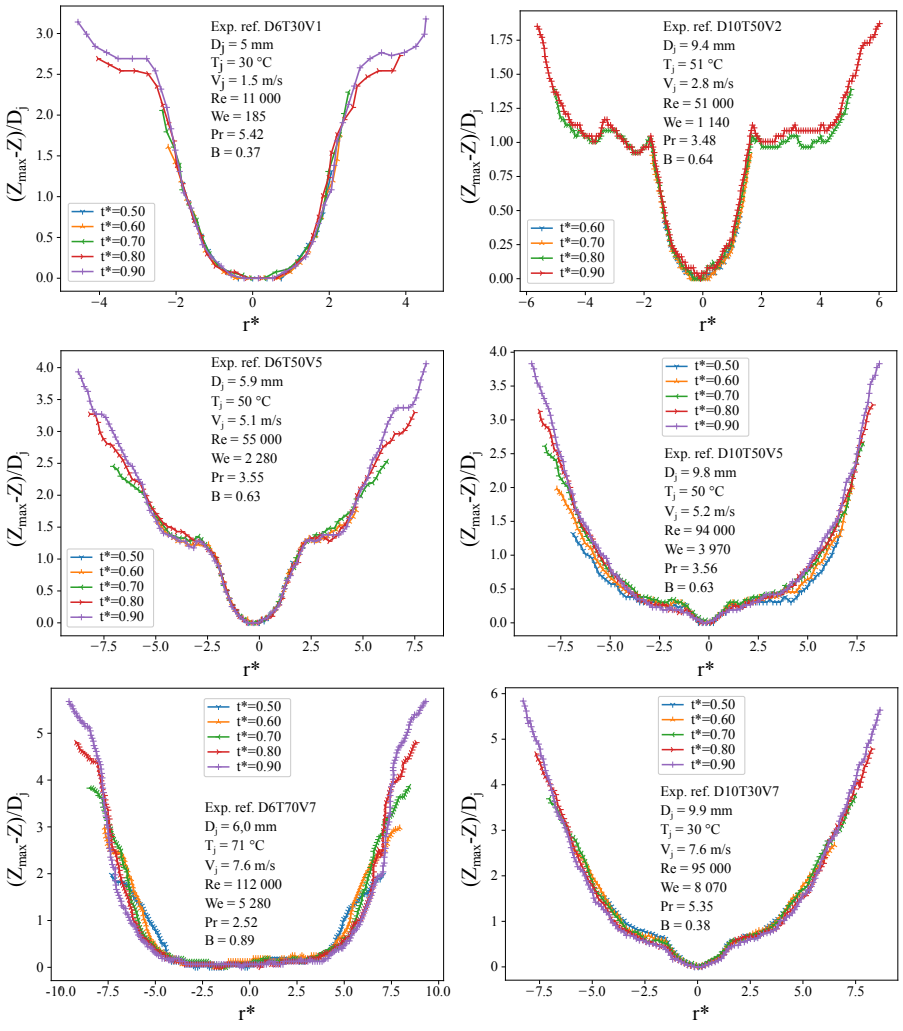

Figure 3: Dimensionless contour evolution with dimensionless time t^* during film regime for six experiments representative of the different cavity shapes encountered. $\frac{Z_{max}-Z}{D_j}$ is the height of a point on the cavity interface measured from cavity deepest point and resized by jet diameter. Likewise, $r^* = \frac{r}{D_j}$ is the radial distance from jet axis scaled by jet diameter.

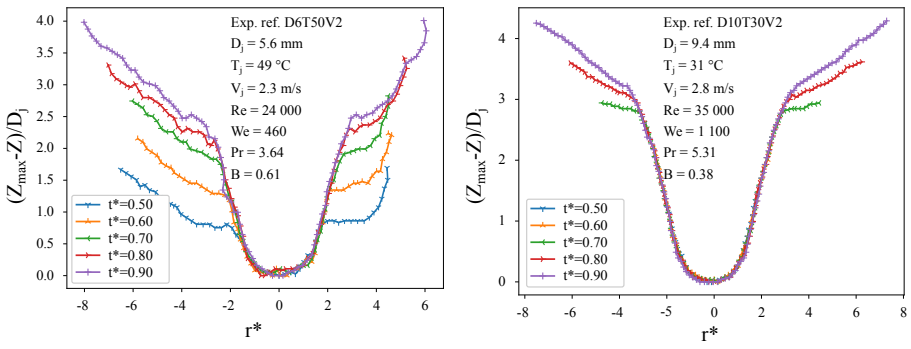

Figure 4: Dimensionless contours for which a different behavior is observed.

5. Evolution of cavity shape with Reynolds number

. Position of the plateau relative to the stagnation zone evolves with Reynolds number – *cf.* Fig. 3. To quantify this evolution, we have classified the experiments based on whether the stagnation zone is clearly distinguishable from the plateau. The condition retained is the ability to measure a lateral angle α for the approximate truncated cone shape joining the stagnation zone and the plateau. An example of such a measure is given in Fig. 5. Experiments thus classified, represented in the Reynolds Number / melting number domain are available in Fig. 6. A clear limit between the two types of cavities emerges at $Re = 66\ 500$. A limit based on the Reynolds number indicates that the evolution is governed by hydrodynamics of the flowing film.

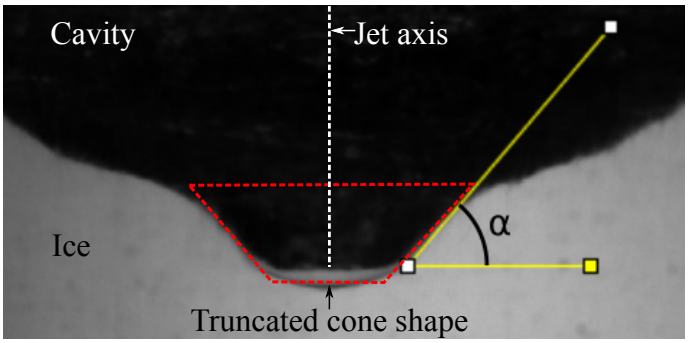

Figure 5: Picture of the cavity. The truncated cone shape is outlined with a red dashed line. An example of truncated cone shape lateral angle α measurement with Fiji software [35] is pictured as yellow lines.

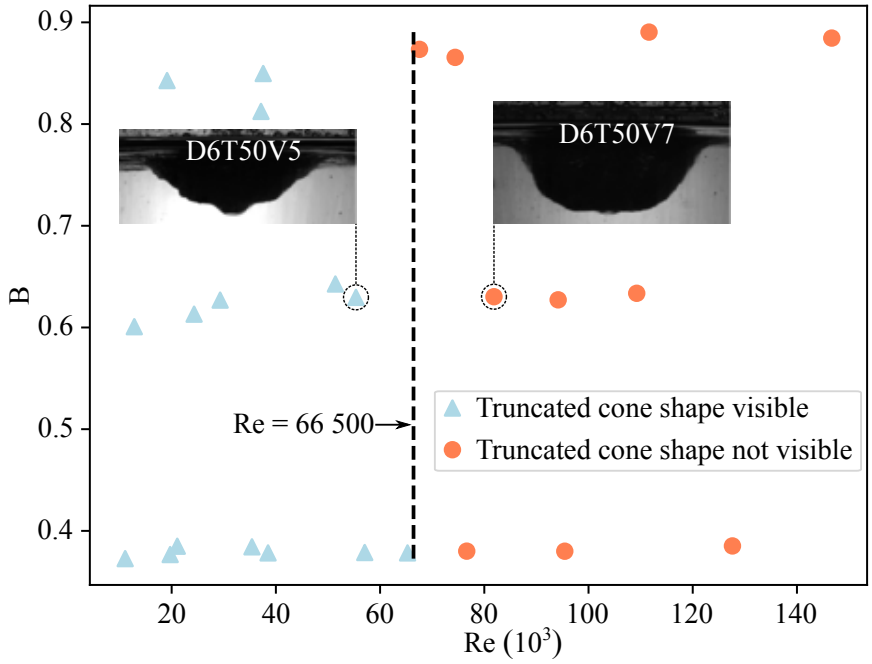

Figure 6: Experiments classification in the *Re* / *B* domain based on truncated cone shape visibility.

6. Dynamics of liquid exit

. From experiments performed in HAnSoLO, we have noted that in film ablation regime, liquid may exit the cavity in different ways. Three ways were identified. Examples of these ways are given in Fig. 7. The liquid may follow the solid surface. It may also detach from the solid and form a coherent liquid sheet. When a coherent liquid sheet forms, then it often disappears and liquid then exits the cavity as a fragmented liquid sheet. Finally, in some cases, no coherent liquid sheet forms and the fluid leaves the cavity as a fragmented liquid sheet from the beginning of the experiment; this is the third way of exit we have noted.

. Experiments classification based on liquid exit state is given in table 1. The two dimensionless numbers influencing liquid exit state are Reynolds and We-

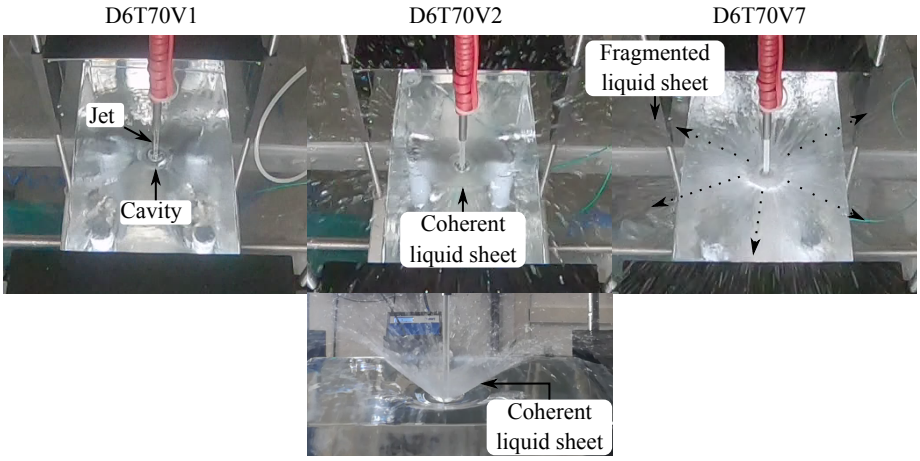

Figure 7: Examples for the three liquid exit modes witnessed. D6T70V1: liquid follows the solid boundary. D6T70V2: the liquid film first follows over the solid boundary, then forms a coherent liquid sheet ($t^* = 0.3$) it finally turns into a fragmented liquid sheet ($t^* = 0.60$). D6T70V7: liquid exits cavity as a fragmented liquid sheet.

ber numbers. Experiments location in the Reynolds number / Weber number domain is available in Fig. 8. To improve diagram legibility, zooms of Fig. 8, on the zones where no fragmented liquid sheet forms and where the liquid film stays in contact with the solid throughout the film ablation regime, are available in the appendix Fig. 19. Experiments classification is highlighted in the figures and the three experiments used as examples in Fig. 7 are identified. Two clear limits are visible. $We = 400$ separates experiments for which liquid follows over the solid surface, from the ones for which a coherent liquid sheet forms. Likewise, $Re = 56\ 000$ separates experiments for which a coherent liquid sheet forms, from the ones for which liquid leaves the cavity as a totally fragmented sheet.

A condition on the Weber number for the existence of a coherent liquid sheet can be explained by the fact that in order to form a coherent liquid sheet liquid / air interface must be created. The second condition on the Reynolds number may indicate that turbulence in the liquid sheet is the destabilizing agent leading to the transition to a fragmented liquid sheet.

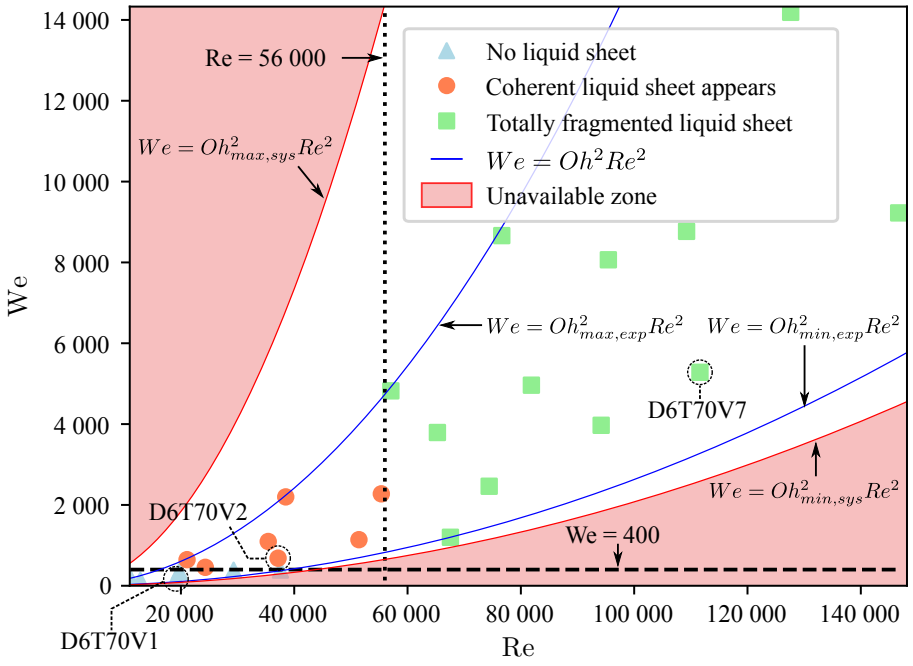

Figure 8: Experiments positions in the Re / We domain. Experiments are sorted based on liquid exit state as listed in table 1. The unavailable zone on HAnSoLo is colored in light-red. Zooms are available in appendix: Fig. 19.

. It is interesting to note that all the positions in the Reynolds number (Re) / Weber number (We) domain are not available with HAnSoLO facility. Weber and Reynolds numbers are linked by the Ohnesorge number (Oh) following Eq. (5).

$$Oh = \frac{\sqrt{We}}{Re} = \frac{\mu_j}{\sqrt{\rho_j \sigma_j D_j}} \tag{5}$$

The Ohnesorge number (Oh) compares viscous forces to surface tension effects. It depends on the temperature, on the jet diameter and is independent of jet velocity. Minimum and maximum experimental values are given in table 2 along with the technical limits of HAnSoLO facility[6]. Experimental limits

[6]HAnSoLO was built to operate with water.

on Ohnesorge number (Oh) are computed using the minimum and maximum values reached in HAnSoLO for this set of experiments, that is $T_j = 71\ ^oC$ and $D_j = 10\ mm$ to compute $Oh_{min,exp}$, and $T_j = 30\ ^oC$ and $D_j = 4.8\ mm$ to compute $Oh_{max,exp}$. For completeness sake, technical limits on Ohnesorge number (Oh) are also computed using the minimum and maximum values reachable in HAnSoLO, namely $T_j = 80\ ^oC$ and $D_j = 10\ mm$ to compute $Oh_{min,sys}$ and $T_j = 20\ ^oC$ and $D_j = 3\ mm$ to compute $Oh_{max,sys}$. Though technically possible, these values have not been reached since there is currently no 3 mm nozzle, and we chose to avoid working at ambient temperature to have better control over jet temperature.

Table 2 shows that each experimental limit – maximum or minimum – on Ohnesorge number is of the same order of magnitude as the technical limit.

Eq. (5), in conjunction with technical limits on Ohnesorge number given in table 2, defines a zone which is unavailable with HAnSoLO. This unavailable zone is pictured in Figs. 8 & 19. Likewise, the limits defined by the minimum and maximum experimental values of the Ohnesorge number are pictured as blue lines in Figs. 8 & 19.

Fig. 8 shows that our data points cover most of the technically available domain in HAnSoLO.

Liquid sheet	Exp. ref.	Re	We	t^*
No	D6T30V1	11 000	185	-
	D6T50V1	13 000	131	
	D6T70V1	19 000	170	
	D10T30V1	19 000	347	
	D10T50V1	29 000	385	
	D10T70V1	38 000	388	
Yes coherent	D6T30V2	21 000	646	$0.44 - 0.72$
	D6T30V5	29 000	2 299	$0.15 - 1$
	D6T50V2	24 000	456	$0.52 - 0.73$
	D6T50V5	55 000	2 274	$0.20 - 0.28$
	D6T70V2	37 000	682	$0.31 - 0.60$
	D10T30V2	35 000	1 095	$0.31 - 1$
	D10T50V2	51 000	1 140	$0.34 - 0.52$
Yes fragmented	D6T30V7 614	57 000	4 823	-
	D6T30V10	77 000	8 663	
	D6T50V7	82 000	4 963	
	D6T50V10	109 000	8 769	
	D6T70V5	74 000	2 462	
	D6T70V7	112 000	5 282	
	D6T70V10	147 000	9 225	
	D10T30V5	65 000	3 792	
	D10T30V7	95 000	8 065	
	D10T30V10	128 000	14 188	
	D10T50V5	94 000	3 970	
	D10T70V2	68 000	1 200	

Table 1: Experiments classification based on liquid exit mode. Reynolds and Weber numbers are reported for each experiment, along with the existence interval of the coherent liquid sheet if applicable. The three modes correspond to the examples given in Fig. 7. Complementary data on each experiment are available in tables 3 and 4.

	Minimum	Maximum
Experimental	$Oh_{min,exp} = 5.1 \cdot 10^{-4}$	$Oh_{max,exp} = 1.2 \cdot 10^{-3}$
Technical	$Oh_{min,sys} = 4.6 \cdot 10^{-4}$	$Oh_{max,sys} = 2.1 \cdot 10^{-3}$

Table 2: Ohnesorge number minimum and maximum values reached experimentally, and technically reachable in HAnSoLO facility. Technical limits are computed using 20 ^oC and 3 mm for minimum jet temperature and diameter, and 80 ^oC and 10 mm for maximum jet temperature and diameter, in accordance with [18]. Experimental limits are computed using 30 ^oC and 4.8 mm for minimum jet temperature and diameter, and 71 ^oC and 10 mm for maximum jet temperature and diameter in accordance with 3.

7. Surface temperature evolution

. In HAnSoLO setup, an infrared (IR) camera – Optris Xi400 – records the ablation process from above. Two examples of IR images are available in Fig. 9. The IR camera allows for liquid / air interface temperature measurement during ablation. We have not identified in the literature that such data were already obtained. These data were analyzed in order to extract data on hydrodynamics. First, a temperature profile was extracted along a measurement line crossing jet axis for each experiment analyzed. Measurement line is pictured in left IR image of Fig. 9. Due to technical issues coming from splashing and coherent liquid sheet, temperature profiles were extracted for the following experiments – *cf.* table 3 –, uncertainty on position scaled by jet diameter is reported in parentheses: D6T30V1 (4 %), D6T30V10 (11 %), D6T50V5 (11 %), D6T70V1 (8 %), D6T70V7 (2 %), D10T30V1 (6 %), D10T30V7 (11 %) and D10T50V5 (6 %). Uncertainty on recorded temperature is of 2 ^oC. For the analysis, temperature difference between the recorded one and the solid temperature scaled by the maximum difference, $\frac{T-T_s}{T_{max}-T_s}$ is used. Also, radial distance from jet axis is scaled by jet diameter, $r^* = \frac{r}{D_j}$.

. First, temperature profiles evolution with time were analyzed. To do so, temperature profiles taken at $t^* = 0.5$ and $t^* = 0.75$ were superimposed for each experiment analyzed. An example is given in Fig. 10 for experiment D6T50V5. For experiment D6T50V5, $t^* = 0.5$ and $t^* = 0.75$ correspond to 7.6 s and 11.5 s from the initial impact of the jet onto the solid. Temperature profiles for a given experiment at different t^* overlap. It means that heat transfers do not change throughout ablation phenomena in film regime. It implies that liquid film hydrodynamic does not change either.

. Then, temperature profiles recorded for different experiments were compared, *cf.* Figs. 11, 12 and 13. In these three figures, experiment D6T50V5 is used as a reference to allow for comparisons across the three graphs. The represented temperature profiles are the ones obtained at $t^* = 0.5$. A plateau is present on

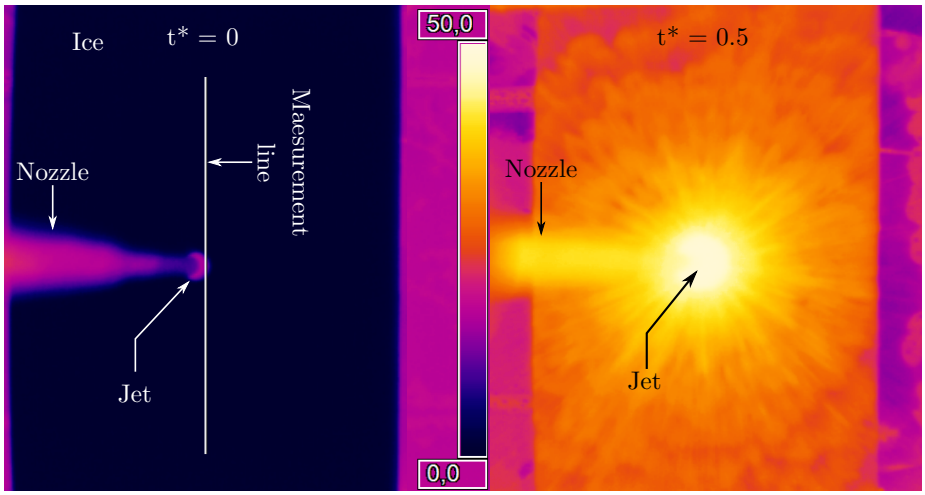

Figure 9: (Left) Visualization from IR camera at time of jet impact on the ice block, $t^* = 0$. Measurement line, along which presented temperature profiles (*cf.* Figs. 10, 11, 12 and 13) are taken, is represented. (Right) IR camera measurement for the same experiment (D6T50V5) at $t^* = 0.5$.

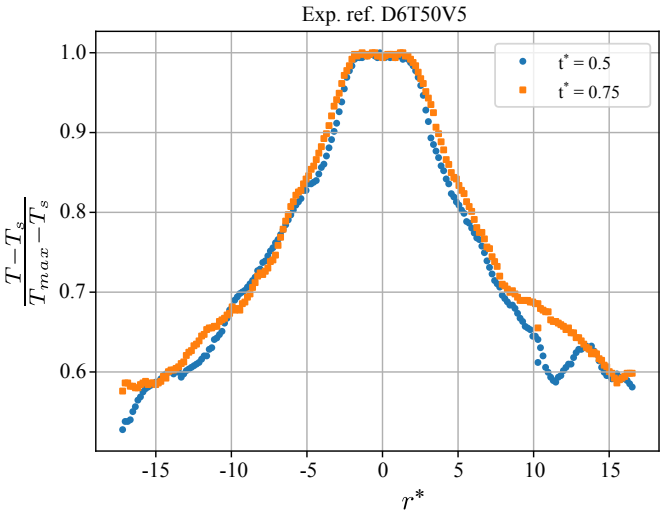

Figure 10: Evolution of dimensionless surface temperature as a function of r^* for two different dimensionless times. The difference in time between the two profiles is of 3.9 s.

all temperature profiles around jet impact. This plateau extends further than jet radius and is due to the fact that the influence of heat transfers at solid / liquid needs time to reach the liquid film surface. This influence may reach the film surface because the thermal boundary layer reach the film. Another possibility is that the film becomes turbulent and better mixing occurs throughout film height, inducing a change in film surface temperature. The following analysis aims at determining which of these explanations is correct.

. Fig. 11 shows the temperature profiles for the three experiments analyzed and conducted with $Re \geqslant 55\ 000$, and a nozzle diameter of 6 mm. The temperature profiles overlap. Likewise, the temperature profiles recorded for experiments D10T50V5 and D10T30V7 are compared to the one recorded for experiment D6T50V5 in Fig. 12. For experiment D10T50V5, $Re = 94\ 000$, for experiment D10T30V7, $Re = 95\ 000$ – both were performed with a jet diameter of 10 mm. For a given jet diameter and $Re \geqslant 55\ 000$, the temperature profile is the same regardless of jet temperature or velocity. However, for experiments conducted with $Re < 20\ 000$ – *cf.* Fig. 13 –, temperature profiles do not overlap with each other, and more importantly with the one recorded for experiment D6T50V5. It shows that for Reynolds numbers lower than 55 000 the temperature profile is a function of both the jet diameter and the Reynolds number.

. It is important to note that for $Re \geqslant 55\ 000$, the extent of the plateau around jet impact is independent of jet parameters like Reynolds number, melting number or jet diameter and velocity. The end of the plateau is located at $r^* = 1.4 \pm 0.2$ for these experiments. For $Re < 20\ 000$, the extent of the plateau is larger than for $Re \geqslant 55\ 000$. The end of the plateau is located at $r^* = 4.6 \pm 0.6$ in these cases.

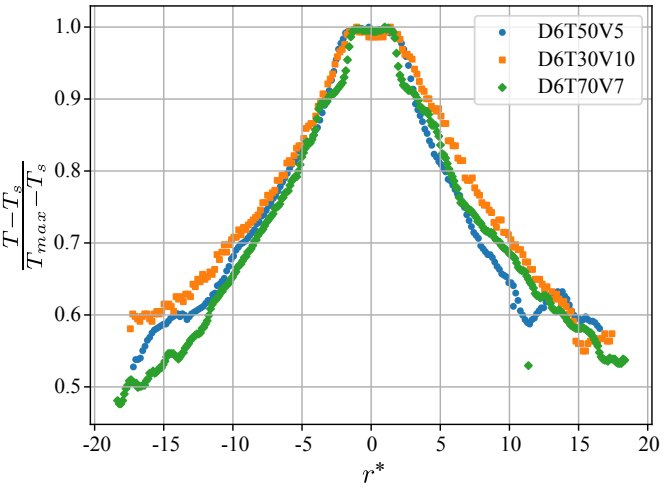

Figure 11: Evolution of dimensionless surface temperature as a function of r^* at $t^* = 0.5$ for three experiments conducted with a nozzle diameter of 6 mm and $Re \geqslant 55\,000$.

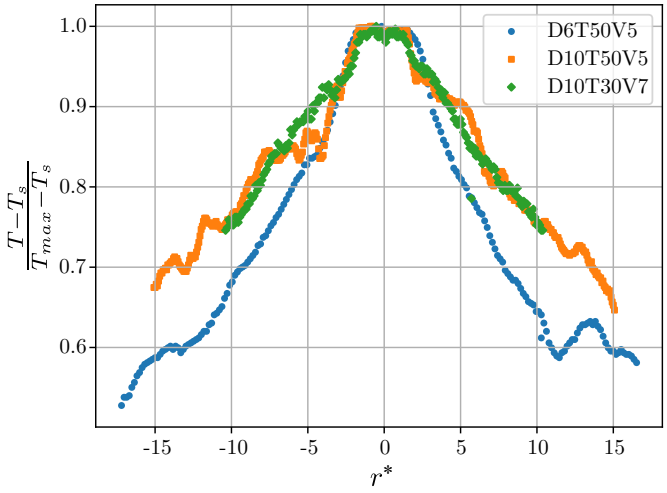

Figure 12: Evolution of dimensionless surface temperature as a function of r^* at $t^* = 0.5$ for experiments D10T50V5 and D10T30V7 conducted with a nozzle diameter of 10 mm. Experiment D6T50V5 is used as reference for comparison with the other temperature profiles obtained with a nozzle diameter of 6 mm, *cf.* Fig. 11.

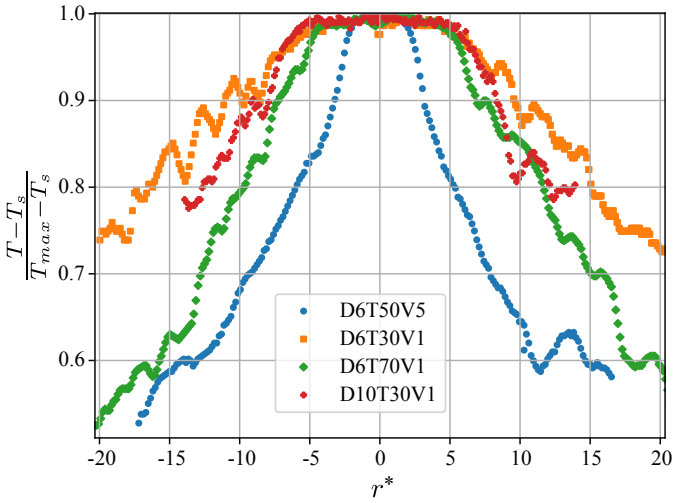

Figure 13: Comparison of dimensionless temperature profiles for three experiments performed with Reynolds numbers below 55 000 (jet velocity below 2.5 $m.s^{-1}$). Experiment D6T50V5 is also reported as reference for comparison with the other temperature profiles, *cf.* Figs. 11 & 12.

8. Explanation of cavity shape in film regime

. In this section an explanation is presented based on the observations reported in the previous sections as well as in a previous paper [18].

We have shown [18] that in our range of jet Reynolds number at impact, the turbulent flow in the jet is laminarized at jet impact. Also, the cavity appears flat around jet impact due to the presence of a stagnation zone. Then, in most cases, further away from jet impact cavity widens and assumes an approximate truncated cone shape. The truncated cone shape ends with an inflection point which may be followed by a plateau before reaching the solid block surface. It was identified that the plateau is in fact a local increase of cavity depth which forms a "W" shape. This "W" shape appears flat in high-speed camera visualization due to projection – shadowgraphy.

. To understand the link between heat transfer, hydrodynamics of the flowing film and cavity shape in film ablation regime, we superimposed the temperature profiles obtained – *cf.* section 7 – with corresponding high-speed camera recording. An example of such a graph is given in Fig. 14. It can be noticed that the end of the flat zone in the temperature profile corresponds with the beginning of the plateau witnessed on cavity shape. It means that before the inflection point, film surface temperature is constant and equal to jet impact temperature. A change in surface temperature means that thermal influence of heat transfers at solid / liquid interface reaches liquid film surface. It can occur either if thermal boundary layer reaches film surface or if better homogenization occurs within the liquid film by means of turbulence. If it were due to boundary layer growth then the radial distance at which film surface temperature decreases should decrease as Reynolds number increases. Instead, we observed that the dimensionless radial distance at which surface temperature changes is independent of the Reynolds number. This is consistent with the results of Stevens *et al.* [36] and of Lienhard [34] concerning turbulent transition of a liquid film produced by the impact of a turbulent liquid jet on a flat plate.

We conclude that the plateau observed is certainly a consequence of turbulent transition of the liquid film.

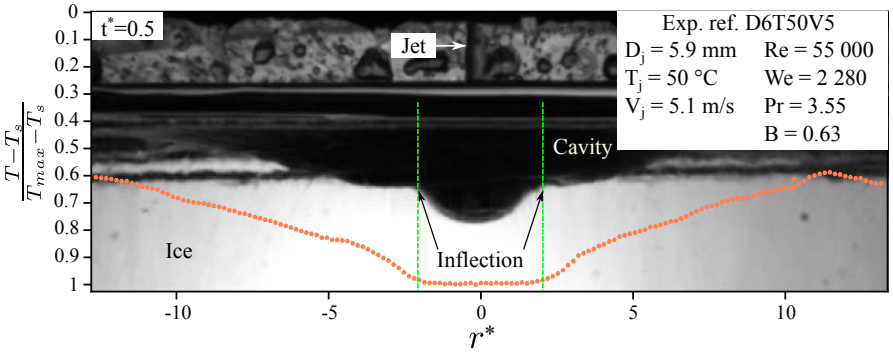

Figure 14: Photograph of cavity shape ($t^* = 0.5$) compared to the dimensionless temperature taken for experiment D6T50V5. Temperature profile is reversed to improve comparison.

. Data are available in the literature [36] for transition toward turbulence of a liquid film formed by the impact of a turbulent jet onto a non-meltable solid surface at right angle. Stevens *et al.* [36] locates the transition at $r^* = 1.75$ for a jet diameter of 5.8 mm. Lienhard [34] gives $r^* = 2.5$. The limits given in previous sections are radial position on a truncated cone shape. In order to compare these value to the conditions given by Stevens *et al.* [36] and Lienhard [34] we assume a truncated cone for cavity shape. We consider a stagnation zone radial extent of $0.75 \times D_j$ and a lateral angle for the truncated cone shape α ranging from 42.6^o to 64.5^o. These two angles are the extreme values measured on experimental cavity shapes – *cf.* Fig. 5. The computed distance between jet impact point and temperature profile decrease ranges from $1.4 \times D_j$ and $2.5 \times D_j$ for tests performed with $Re \geqslant 55\,000$. These values are consistent with the limits given by both Stevens *et al.* [36] and Lienhard [34].

Stevens *et al.* [36] report a local increase in heat transfer at transition toward turbulence. They also show that the increase may be steeper for higher Reynolds numbers. It can explain why the vertical distance between stagnation zone and the inflection point in the cavity shape decreases as Reynolds number

increases – *cf.* Figs. 1 & 14. Indeed, an increase in local heat transfer leads to a deepening of the "W" shape.

. Finally, from our observations we can conclude that the shape of the cavity produced by ablation of an ice block by a water jet recorded in HAnSoLO experiment is mostly dictated by the hydrodynamics of the liquid flowing over the solid. First, the jet impacts onto the solid block; a stagnation point flow produces a stagnation zone with uniform heat transfers. Cavity appears flat. Turbulent flow in the jet is laminarized at impact. Then heat transfers are lowered due to boundary layer growth. Afterward, transition toward turbulence occurs; heat transfers locally increase. Finally, the liquid film becomes fully turbulent, then heat transfers ultimately decrease as temperature difference between the solid and the liquid film decreases.

9. Analysis and model to explain the transition to pool effect

. A first report of data obtained with HAnSoLO on maximal cavity depth at transition toward pool effect, $Z_{max,pe}$, for a single jet diameter is available in [18]. To complement these data, 10 additional experiments were performed with a 10 mm diameter nozzle – *cf.* Fig. 2 & table 3. Data obtained with both nozzle diameters are available in Fig. 15. This graph confirms that $Z_{max,pe}$ increases not only with jet velocity but also with jet diameter. To push the analysis further we have developed a simple physical model.

. Previous analysis hinted that transition between film ablation regime and pool effect is linked to the balance of outgoing radial current and gravity effects [18]. We assumed that for the pool effect to occur, the momentum brought by the jet, and diverted upward by cavity shape, shall not be enough to balance the gravity push of liquid, should the cavity be filled up to the stagnation zone. The physical system thus considered is represented in Fig. 16. The control volume used for the balance is highlighted. We further neglected the effect of pressure and shear stress. Noting, n_p the components of the normal vector, $\mathcal{V}$ the volume

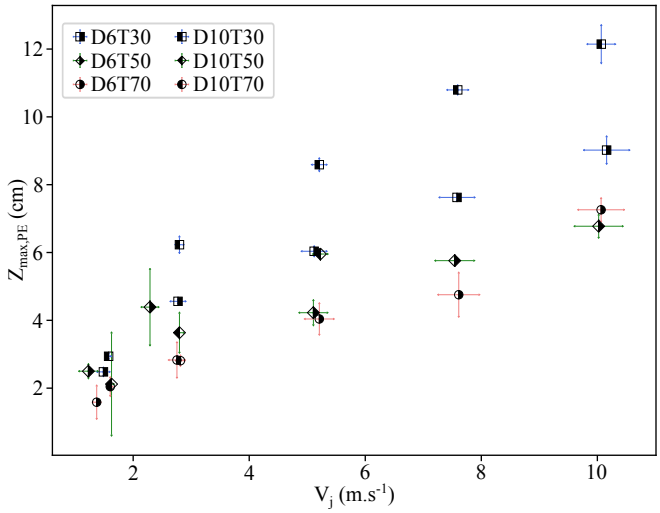

Figure 15: Evolution of maximum cavity depth measured at transition toward pool effect, $Z_{max,pe}$, as a function of jet velocity V_j. Uncertainty intervals on data points are pictured as error bars.

of the control volume and S it corresponding lateral surface, the balance may be written as follows [37]:

$$\iint_S \rho V_i \left(V_p n_p\right) dS = \iiint_{\mathcal{V}} \rho g_i d\mathcal{V} \tag{6}$$

Stagnation zone limit was located at $r^* = \frac{3}{4}$ [36]. Also, we assumed that the height of liquid entrance into the control volume is equal to the height of the liquid film at the end of the stagnation zone, namely $l\left(r_{stag}\right) = l_e$. Equation (6) is projected on the vertical axis. We note V_z the vertical velocity component. We thus obtained, with α the truncated cone shape lateral angle:

$$\iint_S \rho V_z \left(V_p n_p\right) dS = -\frac{\pi}{4} \rho D_j^2 V_j^2 sin(\alpha) \tag{7}$$

$$\iiint_{\mathcal{V}} \rho g_i d\mathcal{V} = -\rho g \pi D_j^3 \left[\frac{3}{4} \frac{Z^{*2}}{tan(\alpha)} + \frac{1}{3} \frac{Z^{*3}}{tan^2(\alpha)}\right] \tag{8}$$

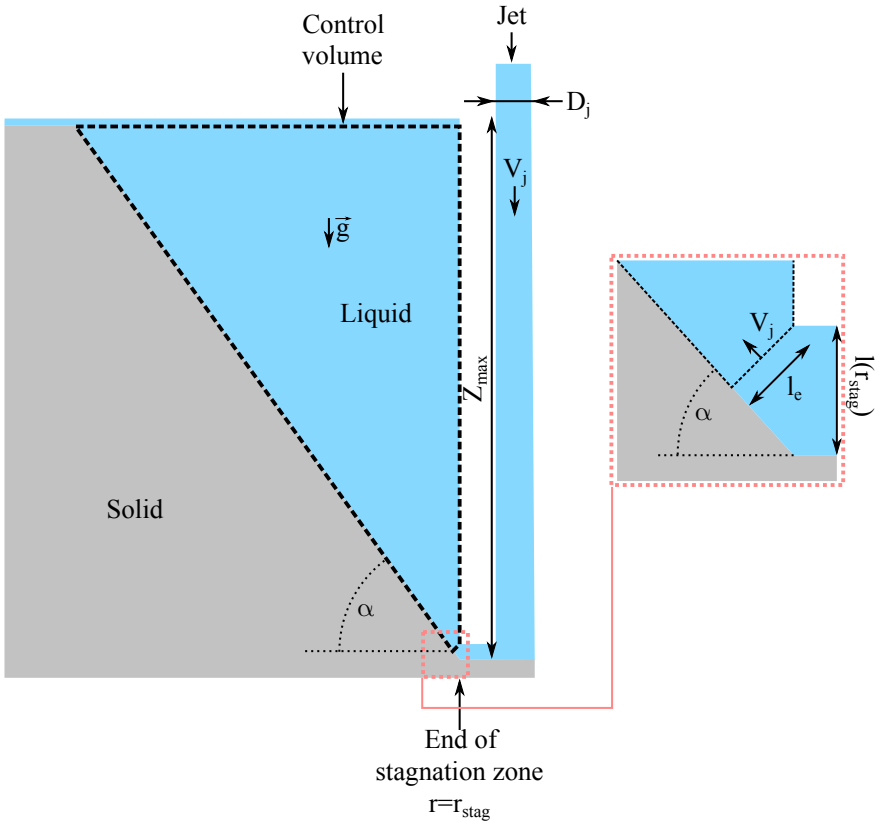

Figure 16: Schematic depiction of the physical system considered to establish the momentum balance leading to pool effect transition model (*cf.* Eq. (10)). Important variables for modeling are represented.

The momentum balance is thus given by the following equation:

$$Z^{*3} + \frac{9}{4} tan(\alpha) Z^{*2} - \frac{3}{4} \frac{sin^3(\alpha)}{cos^2(\alpha)} Fr^2 = 0 \tag{9}$$

455 This model shows the importance of both $Z^* = \frac{Z}{D_j}$, the cavity depth scaled by jet diameter, and $Fr = \frac{V_j}{\sqrt{gD_j}}$, jet Froude number, for pool effect characterization. An analytical solution is found if the second-order term is neglected,

that is:

$$Z^* = sin(\alpha)\sqrt[3]{\frac{3}{4}\left(\frac{Fr}{cos(\alpha)}\right)^2} \tag{10}$$

This equation demonstrates that, as a first approximation, $Z^* \propto Fr^{2/3}$ at pool effect transition. This criterion gives a condition on the possibility of transition toward pool effect, as it dictates whether the jet is capable of emptying the cavity if it comes to be filled.

. Fig. 17 shows a depiction of data obtained on transition to pool effect in the Fr / Z^* domain. Are also represented results of Eq. (10) for several values of α. No dependency of Z^* on D_j is witnessed. It means that $Z_{max,pe}$ varies with $\sqrt{D_j}$. Dispersion of data points is lower than in Fig. 15. Therefore, Z^* and Fr are the dimensionless numbers which must be used to adequately study pool effect transition. Furthermore, Fig. 17 demonstrates that Eq. (10) gives correct tendencies as well as a valuable lower bound for pool effect transition if $\alpha = 45^o$ is used. This value of 45^o is close to the minimal value of the truncated cone shape that was measured, namely $\alpha = 42.6^o$.

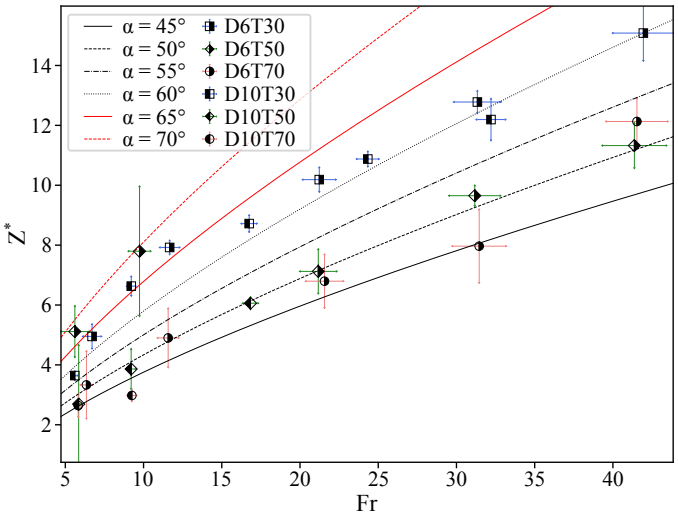

Figure 17: Evolution of dimensionless maximal cavity depth at transition toward pool effect, $Z^* = \frac{Z_{max,pe}}{D_j}$, with jet Froude number, $Fr = \frac{V_j}{\sqrt{gD_j}}$. Uncertainty intervals are pictured by means of error bars. Solutions of the model presented – *cf.* Eq. (10) – are given for six values of α ranging from 45^o to 70^o.

10. Conclusion

. We have proved here that once the cavity assumes a shape in the film ablation regime then that shape is stable up to the transition to pool effect. This implies that heat transfers are established and can be considered to be at quasi-steady state. Cavity shape inspection, in conjunction with surface temperature analysis, revealed that cavity shape is in fact dictated by hydrodynamics in the liquid layer flowing over the solid. At impact point, flow becomes laminar due to the large pressure gradient. A stagnation zone develops with a radial extent akin to what is encountered when no melting occurs. Then, liquid layer stays laminar, heat transfers intensity decreases. Farther, transition toward turbulence occurs with a local increase of heat transfers, which may induce a local increase of cavity depth. This increase is hidden due to projection error when backligthing and shadowgraphy are used. It appears as a spurious plateau during visualizations. Finally, liquid layer is fully turbulent and transfers then decrease as liquid moves away from impact point. This is due to interactions between liquid

and solid – heat transfer, friction.

. Among the goals of the present study, one is to shed light on the important dimensionless parameters needed to address the complex problem of melting of a solid by a free turbulent liquid jet. Those are the following. For heat transfers at impact, Nusselt number (Nu) is paramount and subsequently Reynolds (Re) and Prandtl number (Pr) are too, as is often the case in the study of convective heat transfer. Two other dimensionless parameters occur due to melting. The first is the melting number (B), which is a measure of melting effect on heat transfers. The second is the Stanton number (St), which appears as a quantification of the portion of heat carried by the jet absorbed by melting of the solid.

For cavity shape prediction, we have established that Reynolds number (Re) dictates whether or not the truncated cone shape can be distinguished from the inflection point and plateau. In other words, it quantifies the increase in heat transfers due to transition toward turbulence.

Liquid exit state seems to be dictated by Weber number (We) and Reynolds number (Re). The former which compares inertial forces to surface tension indicates whether liquid will detach from solid surface or not. In other words, if there will be interface creation. The latter seems to dictate, in our case, whether a coherent liquid sheet will form or not.

. Lastly, transition toward pool effect was here studied. New data gathered confirm that cavity depth along jet axis at transition toward pool effect increases with jet velocity and diameter. Physical modeling, based on the premises that radial current generated by jet flow deviation at impact is counteracted by gravity as liquid climbs up the cavity at transition, leads to an expression linking the maximal cavity depth scaled by jet diameter (Z^*) to jet Froude number (Fr). Comparison with experiments reveal that this approach gives relevant tendencies even if it requires the prior knowledge of truncated cone shape lateral angle. It highlights the importance of Fr for pool effect characterization.

. It is the first time to the best of the authors' knowledge that quantitative analysis of cavity shape produced by ablation is carried out. Likewise, it is the first time that heat transfer data, between liquid and air, are gathered in the film regime and used to understand hydrodynamics within the flowing liquid film. These allowed us to give a physical explanation to the cavity shape and evolution. An often overlooked part of the ablation in the film regime is also directly studied here: liquid exit modes. The way the liquid exits the cavity can have an impact on the ablation dynamics outside of the cavity. Finally, a first physical model for transition toward pool effect is achieved.

. Within the scope of ESFR-SMART European project, two prototypical experiments were conducted using stainless steel in JIMEC setup at KIT [38]. The cavity detection is different than ours but may ultimately lead to interesting comparisons with our work.

11. Acknowledgments

The research carried in the frame of the ESFR-SMART project leading to some part of results has received funding from the Euratom research and training program 2014-2018 under grant agreement N° 754501.

References

[1] P. Mouchet, M. Roustan, Caractéristiques et propriétés des eaux – eau pure, eaux naturelles, Tech. Ing. (w110) (2011).

[2] J. Guidez, A. Gerschenfel, J. Bodi, K. Mikityuk, F. Alvarez-Velarde, P. Romojaro, U. Diaz-Chiron, ESFR SMART project conceptual design of in-vessel core catcher, EPJ Web Conf. 247 (2021) 01002. doi:10.1051/epjconf/202124701002.

[3] Reactor Harmonization Group RHWG, Safety of new NPP designs, Tech. rep., Western European Nuclear Regulators Association (Mar. 2013).

URL http://www.wenra.org/media/filer_public/2013/08/23/rhwg_safety_of_new_npp_designs.pdf

[4] F. Bertrand, N. Marie, A. Bachrata, V. Brun-Magaud, J. Droin, X. Manchon, K. Herbreteau, B. Farges, B. Carluec, S. Poumerouly, D. Lemasson, Status of severe accident studies at the end of the conceptual design of ASTRID: Feedback on mitigation features, Nucl. Eng. Des. 326 (2018) 55 – 64. doi:10.1016/j.nucengdes.2017.10.019.

[5] G. Albrecht, F. Huber, E. Jenes, A. Kaiser, W. Schütz, KAJET experiments on pressure-driven melt jets and their interaction with concrete, Tech. Rep. FZKA-7002, KIT (2005). doi:10.5445/IR/270060425.

[6] F. Gauché, Generation IV reactors and the ASTRID prototype: Lessons from the fukushima accident, C. R. Phys. 13 (4) (2012) 365 – 371. doi:10.1016/j.crhy.2012.03.004.

[7] L. Roberts, On the melting of a semi-infinite body of ice placed in a hot stream of air, J. Fluid Mech. 4 (5) (1958) 505–528. doi:10.1017/S002211205800063X.

[8] D. B. Coveney, Cutting ice with high pressure water jets, Tech. Rep. ADA106985, National research council of Canada Ottawa (Ontario) div. of mechanical engineering, Ottawa (Jul. 1981).
URL http://www.dtic.mil/docs/citations/ADA106985

[9] B. R. Koci, Hot water drilling in antarctic firn, and freezing rates in water-filled boreholes, in: G. Holdsworth, K. C. Kuivinen, J. H. Rand (Eds.), Ice drilling technology, Hanover, New Hampshire, USA, 1984, pp. 101 – 117.
URL https://archive.org/details/DTIC_ADA156733

[10] V. A. Morev, V. A. Pukhov, V. M. Yakovlev, V. S. Zagorodnov, Equipment and technology for drilling in temperate glaciers, in: G. Holdsworth, K. C. Kuivinen, J. H. Rand (Eds.), Ice drilling technology, Hanover, New

Hampshire, USA, 1984, pp. 125 – 127.
URL https://archive.org/details/DTIC_ADA156733

[11] R. R. Gilpin, The ablation of ice by a water jet, Trans. Can. Soc. Mech. Eng. 2 (2) (1973) 91 – 96. doi:10.1139/tcsme-1973-0014.

[12] A. Lipsett, Jet impingement heat transfer including effect of melting, Master's thesis, University of Alberta, Edmonton, Alberta (1976).

[13] A. Lipsett, R. R. Gilpin, Laminar jet impingement heat transfer including the effects of melting, Int. J. Heat Mass Transf. 21 (1978) 25 – 33. doi:10.1016/0017-9310(78)90152-7.

[14] M. J. Swedish, M. Epstein, J. H. Linehan, G. A. Lambert, G. M. Hauser, L. J. Stachyra, Surface ablation in the impingement region of a liquid jet, AIChE J. 25 (4) (1979) 630–638. doi:10.1002/aic.690250409.

[15] A. Furutani, S. Imahori, K. Sato, M. Saito, Erosion behavior of a solid plate by a liquid jet - effect of molten layer, Nucl. Eng. Des. 132 (2) (1991) 153 – 169. doi:10.1016/0029-5493(91)90263-H.

[16] M. Saito, K. Sato, A. Furutani, M. Isozaki, S. Imahori, Y. Hattori, Melting attack of solid plates by a high temperature liquid jet — effect of crust formation, Nucl. Eng. Des. 121 (1) (1990) 11 – 23. doi:10.1016/0029-5493(90)90003-G.

[17] K. Sato, A. Furutani, M. Saito, M. Isozaki, K. Suganuma, S. Imahori, Melting attack of solid plates by a high-temperature liquid jet [II] — erosion behavior by a molten metal jet, Nucl. Eng. Des. 132 (2) (1991) 171 – 186. doi:10.1016/0029-5493(91)90264-I.

[18] A. Lecoanet, F. Payot, C. Journeau, N. Rimbert, M. Gradeck, Study of the ablation consecutive to jet impingement on a meltable solid – Application to SFR core-catcher, Nucl. Eng. Des. 377 (2021) 111147. doi:10.1016/j.nucengdes.2021.111147.

[19] O. M. Griffin, Heat, mass, and momentum transfer during the melting of glacial ice in sea water, J. Heat Transfer 95 (3) (1973) 317–323. doi:10.1115/1.3450058.

[20] M. Esptein, The effect of melting on heat transfer to submerged bodies, Lett. Heat Mass Transf. 2 (2) (1975) 97 – 103. doi:10.1016/0094-4548(75)90047-8.

[21] Y.-C. Yen, A. Zehnder, Melting heat transfer with water jet, Int. J. Heat Mass Transf. 16 (1) (1973) 219 – 223. doi:10.1016/0017-9310(73)90265-2.

[22] C. Tien, Y.-C. Yen, The effect of melting on forced convection heat transfer, J. Appl. Meteorol. 4 (4) (1965) 523–527.
URL https://www.jstor.org/stable/26172936

[23] G. Li, M. Liu, J. Wang, D. Chong, J. Yan, Numerical study of thermal erosion behavior of RPV lower head wall impinged by molten corium jet with particle method, Int. J. Heat Mass Transf. 104 (2017) 1060–1068. doi:10.1016/j.ijheatmasstransfer.2016.09.009.

[24] G. Li, M. Liu, J. Wang, D. Chong, J. Yan, Crust behavior and erosion rate prediction of EPR sacrificial material impinged by core melt jet, Nucl. Eng. Des. 314 (2017) 44–55. doi:10.1016/j.nucengdes.2017.01.009.

[25] S. M. An, K. S. Ha, B. T. Min, H. Y. Kim, J. H. Song, Ablation characteristics of special concrete due to an impinging zirconium-dioxide melt jet, Nucl. Eng. Des. 284 (2015) 10–18. doi:10.1016/j.nucengdes.2014.10.024.

[26] A. J. Sudha, M. Kumaresan, J. Anandan, S. S. Murthy, B. Malarvizhi, G. Lydia, D. Ponraju, B. K. Nashine, P. Selvaraj, Experimental simulation of downward molten material relocation by jet ablation of structures and fuel coolant interaction in a fast reactor, Prog. Nucl. Energy 105 (2018) 194–201. doi:10.1016/j.pnucene.2018.01.010.

[27] T. V. Pawar, A. J. Sudha, D. Ponraju, B. K. Nashine, P. Selvaraj, An effective conductivity model for jet ablation of a solid substrate, IOP Conf. Ser.: Mater. Sci. Eng. 402 (2018) 012057. doi:10.1088/1757-899x/402/1/012057.

[28] A. Lecoanet, Étude de l'ablation d'une paroi solide par un jet liquide, Ph.D. thesis, Université de Lorraine (2021).
URL http://www.theses.fr/2021LORR0015

[29] A. Lecoanet, N. Rimbert, M. Gradeck, F. Payot, Ablation d'un bloc de glace transparente par un jet d'eau chaude – Application à la sûreté des RNR-Na, Entropie 1 (4) (2020). doi:10.21494/ISTE.OP.2020.0519.

[30] X. Liu, J. H. Lienhard, V. J. S. Lombara, Convective heat transfer by impingement of circular liquid jets, J. Heat Transfer 113 (3) (1991) 571–582. doi:10.1115/1.2910604.

[31] A. Y. Tong, A numerical study on the hydrodynamics and heat transfer of a circular liquid jet impinging onto a substrate, Numer. Heat Tr. A-Appl. 44 (1) (2003) 1–19. doi:10.1080/713838171.

[32] S. van der Walt, J. L. Schönberger, J. Nunez-Iglesias, F. Boulogne, J. D. Warner, N. Yager, E. Gouillart, T. Yu, the scikit-image contributors, scikit-image: image processing in python, PeerJ 2 (2014) e453. doi:10.7717/peerj.453.

[33] F. Payot, C. Journeau, C. Suteau, F. Serre, M. Gradeck, N. Rimbert, A. Lecoanet, A. Miassoedov, A new experimental R&D program associated with the corium jet impingement on the ASTRID core catcher sacrificial material, in: Proc. of ICAPP 2018, ANS, Charlotte, NC, USA, 2018, pp. 657–666. doi:10.5281/zenodo.1309374.

[34] H. J. V. Lienhard, Annual review of heat transfer, in: C.-L. Tien (Ed.), Annual Review of heat transfer, Vol. 6, Begell house inc., New York,

Wallingford (U.K.), 1995, Ch. Liquid jet impingement, pp. 199 – 270. doi:10.1615/AnnualRevHeatTransfer.v6.60.

[35] J. Schindelin, I. Arganda-Carreras, E. Frise, V. Kaynig, M. Longair, T. Pietzsch, S. Preibisch, C. Rueden, S. Saalfeld, B. Schmid, J.-Y. Tinevez, D. J. White, V. Hartenstein, K. Eliceiri, P. Tomancak, A. Cardona, Fiji: an open-source platform for biological-image analysis, Nat. Methods 9 (7) (2012) 676–682. doi:10.1038/nmeth.2019.

[36] J. Stevens, B. W. Webb, Local heat transfer coefficients under an axisymmetric, single-phase liquid jet, J. Heat Transfer 113 (1) (1991) 71–78. doi:10.1115/1.2910554.

[37] E. Guyon, J.-P. Hulin, L. Petit, Hydrodynamique physique, 3rd Edition, EDP Sciences, Les Ulis, FR, 2012, Ch. Équations de bilan, pp. 191 – 224.

[38] A. Lecoanet, M. Gradeck, X. Gaus-Liu, T. Cron, B. Fluhrer, F. Payot, C. Journeau, N. Rimbert, Ablation of a solid material by high temperature liquid jet impingement: an application to corium jet impingement on a SFR core-catcher, ASME J. of Nuclear Rad. Sci. (2021). doi:10.1115/1.4051448.

[39] C. H. Li, C. K. Lee, Minimum cross entropy thresholding, Pattern Recognit 26 (4) (1993) 617–625. doi:10.1016/0031-3203(93)90115-D.

[40] W. E. Lorensen, H. E. Cline, Marching cubes: A high resolution 3D surface construction algorithm, ACM SIGGRAPH Computer Graphics 21 (4) (1987) 163–169. doi:10.1145/37402.37422.

12. Appendix : Experimental conditions and uncertainties

Exp. ref.	T_j ^oC	V_j $m.s^{-1}$	D_j mm	Re $\times 10^3$	Pr	B	We	Fr
D6T30V1	30	1.5	5.0	11	5.42	0.37	190	6.7
D6T30V2	31	2.8	5.8	21	5.30	0.38	650	11.7
D6T30V5	30	5.1	6.0	39	5.37	0.38	2 200	21.2
D6T30V7	30	7.6	6.0	57	5.36	0.38	4 820	31.3
D6T30V10	30	10.2	6.0	77	5.35	0.38	8 660	42.0
D6T50V1	48	1.2	4.9	13	3.70	0.60	130	5.6
D6T50V2	49	2.3	5.6	24	3.64	0.61	460	9.7
D6T50V5	50	5.1	5.9	55	3.55	0.63	2 270	21.2
D6T50V7	50	7.5	6.0	82	3.55	0.63	4 960	31.2
D6T50V10	51	10.0	6.0	109	3.53	0.63	8 770	41.4
D6T70V1	67	1.4	4.8	19	2.67	0.84	170	6.4
D6T70V2	65	2.8	5.8	37	2.77	0.81	680	11.6
D6T70V5	69	5.2	5.9	74	2.60	0.87	2 460	21.6
D6T70V7	71	7.6	6.0	112	2.52	0.89	5 280	31.5
D6T70V10	71	10.1	6.0	147	2.54	0.88	9 230	41.5
D10T30V1	30	1.6	8.1	19	5.38	0.38	350	5.6
D10T30V2	31	2.8	9.4	35	5.31	0.38	1 100	9.2
D10T30V5	30	5.2	9.8	65	5.37	0.38	3 790	16.8
D10T30V7	30	7.6	9.9	95	5.35	0.38	8 070	24.3
D10T30V10	31	10.1	10.0	128	5.30	0.39	14 190	32.2
D10T50V1	50	1.6	7.9	29	3.56	0.63	390	5.85
D10T50V2	51	2.8	9.4	51	3.48	0.64	1 140	9.2
D10T50V5	50	5.2	9.8	94	3.56	0.63	3 970	16.8
D10T70V1	68	1.6	7.7	38	2.65	0.85	390	5.8
D10T70V2	70	2.8	9.4	68	2.57	0.87	1 200	9.3

Table 3: Important input parameters and corresponding dimensionless numbers for the experiments analyzed here. Exp. ref.: experiment reference, T_j: jet temperature, V_j: jet velocity, D_j: jet diameter, Re: Reynolds number, Pr: Prandtl number, B: melting number, We: Weber number, Fr: Froude number. Dimensionless numbers expressions are summarized in nomenclature.

Exp. ref.	ΔV_j $m.s^{-1}$	ΔD_j μm	ΔRe $\times 10^3$	ΔPr	ΔB	ΔWe	ΔFr
D6T30V1	0.10	170	1.3	0.29	0.03	26	0.5
D6T30V2	0.12	91	2.0	0.29	0.03	65	0.6
D6T30V5	0.20	96	3.7	0.29	0.03	217	1.0
D6T30V7	0.29	98	5.5	0.29	0.03	469	1.5
D6T30V10	0.37	99	7.3	0.29	0.03	829	1.9
D6T50V1	0.14	37	2.4	0.16	0.04	34	0.9
D6T50V2	0.13	100	2.5	0.16	0.04	60	0.7
D6T50V5	0.23	97	5.2	0.16	0.04	252	1.1
D6T50V7	0.32	98	7.6	0.16	0.04	533	1.6
D6T50V10	0.40	99	9.9	0.15	0.04	898	2.0
D6T70V1	0.06	120	1.4	0.10	0.04	15	0.3
D6T70V2	0.12	94	3.2	0.11	0.04	75	0.6
D6T70V5	0.23	98	6.7	0.10	0.04	278	1.2
D6T70V7	0.34	99	10	0.09	0.04	594	1.7
D6T70V10	0.38	99	12	0.09	0.04	913	1.9
D10T30V1	0.03	80	1.1	0.29	0.03	14	0.1
D10T30V2	0.06	85	2.4	0.28	0.03	58	0.2
D10T30V5	0.11	95	7.8	0.29	0.03	218	0.5
D10T30V7	0.17	98	7.1	0.29	0.03	475	0.7
D10T30V10	0.23	99	9.5	0.28	0.03	847	0.9
D10T50V1	0.03	76	1.4	0.16	0.04	15	0.1
D10T50V2	0.06	86	3.1	0.15	0.04	62	0.2
D10T50V5	0.11	94	6.0	0.16	0.04	229	0.4
D10T70V1	0.03	80	1.6	0.10	0.04	15	0.1
D10T70V2	0.06	87	3.8	0.10	0.04	68	0.3

Table 4: Absolute uncertainties on parameters of table 3. Uncertainty on jet temperature is of 2 ^oC.

13. Appendix: Image processing algorithm

. To extract cavity contours for further analysis an image processing algorithm was designed, which used Python 3 and Scikit-Image [32]. An illustration of the course of analysis is given by Fig. 18. It proceeds as follows:

0. The region of interest is defined.
1. A map of background intensity is computed by taking average intensities of images obtained before jet impact on the block.
2. For a given time, an equivalent image is computed by taking the average of 20 images. This operation improves solid / liquid interface contrast.
3. Background intensity is removed from the image obtained by subtraction pixel by pixel.
4. Segmentation between pixels inside and outside of the cavity is achieved via thresholding. The resulting image is binarized. Value of pixels inside the cavity is set to 1 (white), value of the others is set to 0 (black). A fixed threshold on intensity of 20 is used in most cases, it was determined empirically using Fiji [35]. This method is not the best one when significant moisture is disrupting visualization. In this case Li's *et al.* [39] filter is used instead. Pixels thus detected do not form a single continuous surface – *cf.* Fig. 18. This is a problem for contour extraction.
5. Continuous groups of white pixels of size smaller than 64 px are removed – *cf.* Fig. 18 image 4 red dashed circle. Artifacts that may be produced during thresholding are thus removed. A continuous surface of pixels must now be constructed.
6. Morphological dilation is performed to bridge together remaining groups of white pixels.
7. Holes are filled, that is, groups of black pixels surrounded by white pixels are considered to be inside the cavity and their value is set to 1 (white).
8. To avoid overestimating cavity surface and retrieve the actual cavity contour, morphological erosion is performed. The structural element is the

same for both dilation and erosion. It is a disk, which radius is determined empirically case by case.

9. Finally, the contour is determined using a scikit-image routine finding the contour[7]. It computes the iso-value line which corresponds to a given level of intensity. It is based on marching squares algorithm [40]. Since the image was binarized after thresholding, a level of 0.5 is used. An example of such an iso-value line is presented in Fig. 18 image 9, it is superimposed with the picture taken with high-speed camera. Good agreement was found between the detected and the genuine cavity contour for every test analyzed here.

. To assess cavity contour evolution with time, coordinates of contour points extracted are converted from pixels to centimeters – Fig. 3 & 4. The conversion rule is determined beforehand on an image of two rulers placed orthogonal. Position of each 1 cm mark is noted. Average and standard deviation on these measures give the conversion sought, the associated uncertainty as well as a hint on potential optical deformations. In all the experiments performed, the standard deviation on pixels to centimeter conversion was always below 1 px, which is not possible if there were optical deformations.

[7]The routine is *measure.find_ contours* from scikit-image 0.17.2.

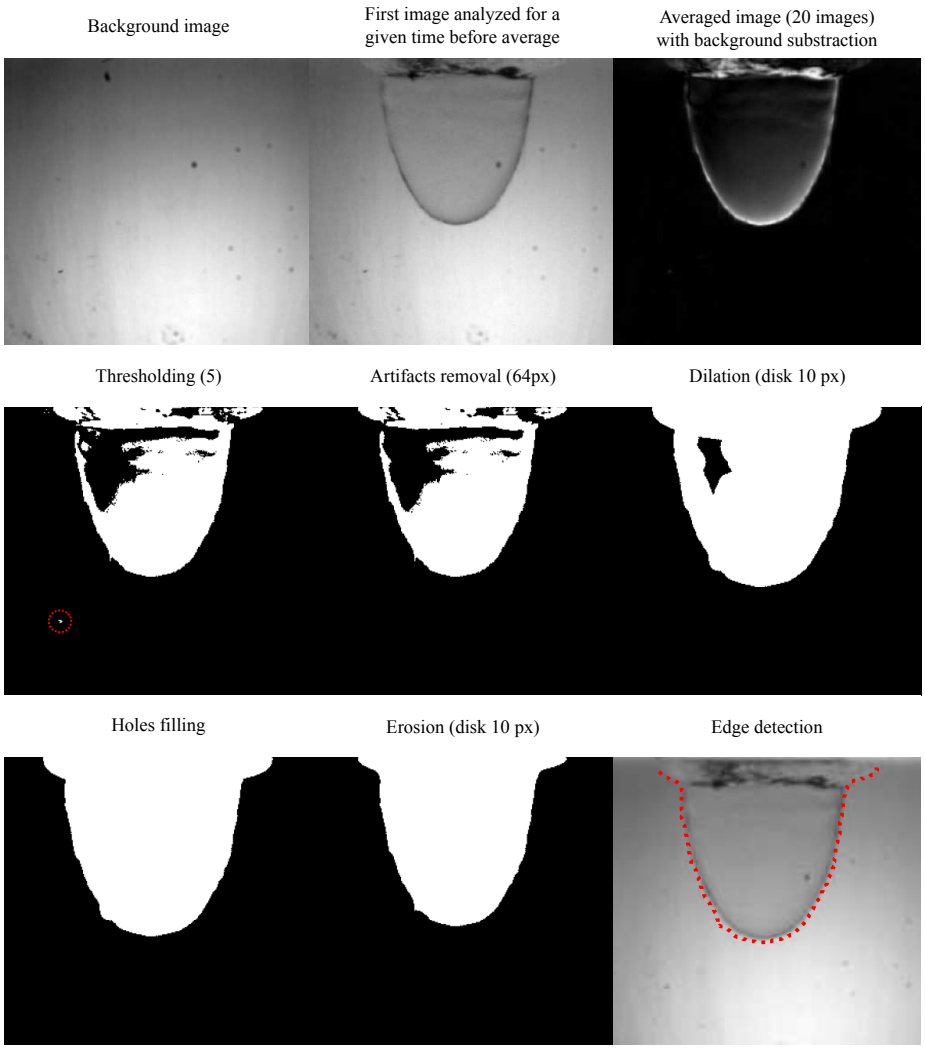

Figure 18: Illustration of the image analysis procedure used to extract cavity contours. Analysis progression starts with the top left picture then proceeds from left to right and from top to bottom. On picture 4 an artifact removed in step 5 is circled. In the last picture (9) the detected contour – red dashed line – is superimposed with the photograph taken by the high-speed camera at corresponding time. Photographs used here correspond to experiment D6T70V1 at $t^* = 4.6$.

14. Appendix: Zooms of Fig. 8

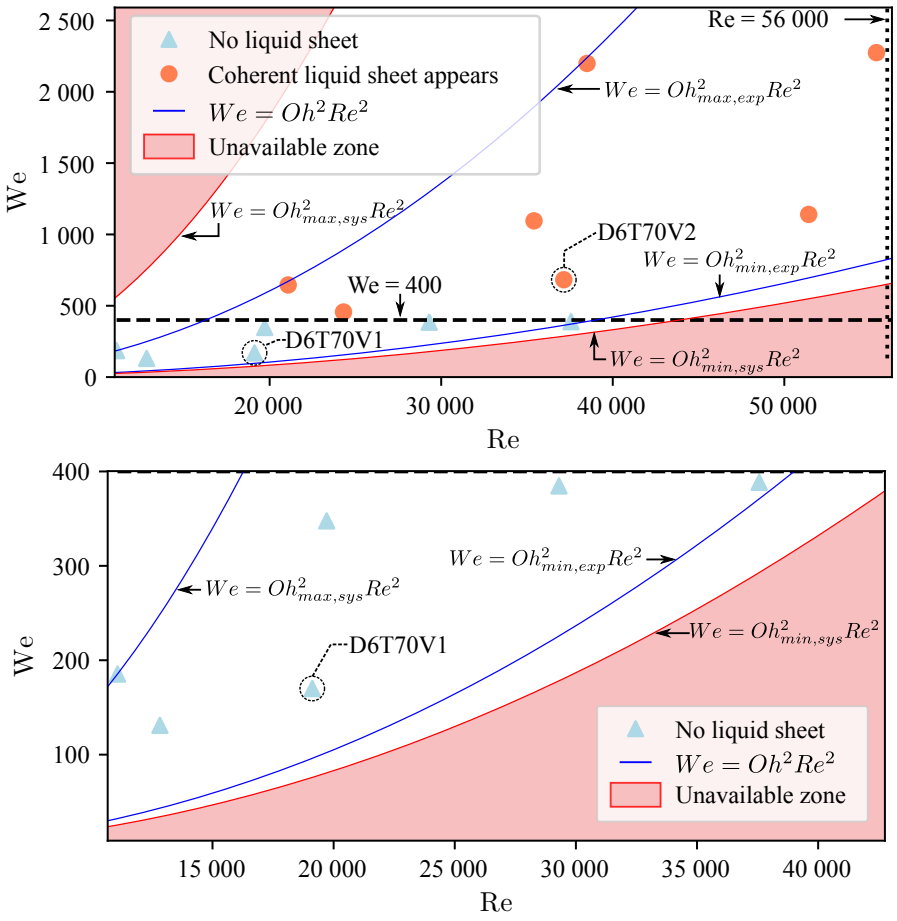

Figure 19: Zooms of Fig. 8 on the coherent liquid sheet existence domain (upper graph), and on the domain where liquid stays attached to the solid boundary (lower graph).